

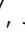





## Sulforaphane exhibits antiviral activity against pandemic SARS-CoV-2 and seasonal HCoV-OC43 coronaviruses in vitro and in mice

Alvaro A. Ordonez <sup>1,2</sup>✉, C. Korin Bullen <sup>2,3</sup>, Andres F. Villabona-Rueda<sup>4</sup>, Elizabeth A. Thompson<sup>5,6</sup>, Mitchell L. Turner<sup>1,2</sup>, Vanessa F. Merino <sup>7</sup>, Yu Yan<sup>7</sup>, John Kim<sup>2</sup>, Stephanie L. Davis <sup>2,3</sup>, Oliver Komm<sup>2,3</sup>, Jonathan D. Powell<sup>5,6</sup>, Franco R. D'Alessio<sup>4</sup>, Robert H. Yolken<sup>8</sup>, Sanjay K. Jain <sup>1,2</sup> & Lorraine Jones-Brando <sup>8</sup>✉

Severe Acute Respiratory Syndrome Coronavirus 2 (SARS-CoV-2), the cause of coronavirus disease 2019 (COVID-19), has incited a global health crisis. Currently, there are limited therapeutic options for the prevention and treatment of SARS-CoV-2 infections. We evaluated the antiviral activity of sulforaphane (SFN), the principal biologically active phytochemical derived from glucoraphanin, the naturally occurring precursor present in high concentrations in cruciferous vegetables. SFN inhibited in vitro replication of six strains of SARS-CoV-2, including Delta and Omicron, as well as that of the seasonal coronavirus HCoV-OC43. Further, SFN and remdesivir interacted synergistically to inhibit coronavirus infection in vitro. Prophylactic administration of SFN to K18-hACE2 mice prior to intranasal SARS-CoV-2 infection significantly decreased the viral load in the lungs and upper respiratory tract and reduced lung injury and pulmonary pathology compared to untreated infected mice. SFN treatment diminished immune cell activation in the lungs, including significantly lower recruitment of myeloid cells and a reduction in T cell activation and cytokine production. Our results suggest that SFN should be explored as a potential agent for the prevention or treatment of coronavirus infections.

<sup>1</sup>Division of Infectious Diseases, Department of Pediatrics, Johns Hopkins University School of Medicine, Baltimore, MD, USA. <sup>2</sup>Center for Tuberculosis Research, Johns Hopkins University School of Medicine, Baltimore, MD, USA. <sup>3</sup>Division of Infectious Diseases, Department of Medicine, Johns Hopkins University School of Medicine, Baltimore, MD, USA. <sup>4</sup>Division of Pulmonology, Department of Medicine, Johns Hopkins University School of Medicine, Baltimore, MD, USA. <sup>5</sup>Department of Oncology, Johns Hopkins University School of Medicine, Baltimore, MD, USA. <sup>6</sup>Bloomberg-Kimmel Institute for Cancer Immunotherapy, Johns Hopkins University School of Medicine, Baltimore, MD, USA. <sup>7</sup>Russell H. Morgan Department of Radiology and Radiological Sciences, Johns Hopkins University School of Medicine, Baltimore, MD, USA. <sup>8</sup>Stanley Division of Developmental Neurovirology, Department of Pediatrics, Johns Hopkins University School of Medicine, Baltimore, MD, USA. ✉email: [aordone2@jhmi.edu](mailto:aordone2@jhmi.edu); [lbrando@jhmi.edu](mailto:lbrando@jhmi.edu)

The coronavirus disease 2019 (COVID-19) pandemic has resulted in substantial global morbidity and mortality. While an unprecedented effort has led to the development of highly effective vaccines, many people remain vulnerable to developing severe disease due to inadequate accessibility or unwillingness to be vaccinated, as well as poor immune responses in certain populations. Other therapeutic approaches have also been developed for COVID-19, including early treatments with monoclonal antibodies against Severe Acute Respiratory Syndrome Coronavirus 2 (SARS-CoV-2)<sup>1</sup>, convalescent plasma<sup>2,3</sup>, and antivirals<sup>4</sup>. Immunomodulators have also been utilized to modify disease and prevent mortality<sup>5</sup>. Early intervention after symptom onset has been shown to be most effective in preventing severe disease and hospitalizations<sup>6,7</sup>. Therefore, the ideal therapy should be one that is readily available and easily administered to patients. Among the direct-acting antivirals, molnupiravir and ritonavir-boosted nirmatrelvir (Paxlovid) are the only oral agents currently authorized by the United States Food and Drug Administration for the treatment of patients with COVID-19<sup>7–9</sup>. Additional oral antiviral therapeutics are urgently needed to prevent more severe disease, hospitalization, and death.

The multi-functional phytochemical sulforaphane (SFN) is the isothiocyanate derived from enzymatic hydrolysis of its precursor glucoraphanin, a glucosinolate found in high concentrations in broccoli (*Brassica oleracea italica*) and other cruciferous vegetables. SFN is a potent naturally occurring activator of the transcription factor nuclear factor erythroid 2-related factor 2 (NRF2), with well-documented antioxidant and anti-inflammatory effects<sup>10–12</sup>. Treatment with SFN increased phagocytic activity of alveolar macrophages<sup>13</sup> and reduced lung injury in animal models of acute respiratory distress syndrome (ARDS)<sup>14</sup>. SFN also decreased the levels of IL-6 and viral load in human subjects infected with live attenuated influenza virus<sup>15,16</sup>. Numerous clinical trials utilizing SFN have demonstrated favorable pharmacokinetics after oral dosing and documented excellent tolerability and safety<sup>10,17–19</sup>.

SFN was identified after an exploratory screening of readily available drugs and compounds for efficacy against human coronaviruses. Initial testing was performed in vitro using seasonal coronavirus HCoV-OC43. Subsequently, drugs that exhibited at least moderate activity against HCoV-OC43 were tested in vitro against SARS-CoV-2. We report here that SFN inhibits in vitro HCoV-OC43 and SARS-CoV-2 infections of mammalian cells and appears to have a synergistic interaction with remdesivir. In addition, SFN reduces viral load and pulmonary pathology in a mouse model of SARS-CoV-2 infection.

## Results

### Antiviral effects of SFN against HCoV-OC43 and SARS-CoV-2.

To evaluate the potential virus-inhibitory activity of SFN, Vero C1008 cells were exposed in vitro to SFN for 1–2 h before inoculation with coronaviruses. In this near-simultaneous drug-infection scenario, SFN effectively inhibited both HCoV-OC43 and SARS-CoV-2-Wuhan-Hu-1 virus-associated cell death in non-human primate Vero C1008 cells in a dose-dependent manner revealing comparable median inhibitory concentrations ( $IC_{50}$  = 10  $\mu$ M, 95% CI 4.7–20.4, and 12  $\mu$ M, 95% CI 4.7–30, respectively), and virus selectivity [therapeutic index (TI)<sub>50</sub> = 7 and 7, respectively] (Figs. 1a and 2a; Supplementary Table 1). When the same assay was performed using human diploid fibroblasts, MRC-5, SFN treatment of HCoV-OC43 infection produced similar results ( $IC_{50}$  = 18  $\mu$ M, 95% CI 9.7–33.5, TI<sub>50</sub> = 5) (Fig. 1b). SFN cytotoxicity was also dose-dependent. The median cytotoxic dose (TD<sub>50</sub>) remained within the range of 73–89  $\mu$ M (Figs. 1a, b and 2a). SARS-CoV-2-associated

cytopathogenicity was not evaluated in human cells because viral infection did not result in measurable cell death. Instead, we quantified viral RNA from SARS-CoV-2-infected human intestinal Caco-2 cells treated with SFN. A dose-dependent reduction was observed with an  $IC_{50}$  of 2.4  $\mu$ M (Fig. 2c).

We further evaluated SFN for activity against a second reference strain of SARS-CoV-2 as well as two clinical strains that carry the spike D614G (614G+) substitution that is found in the majority of variants of concern currently in circulation (Fig. 2d)<sup>20</sup>. SFN inhibited USA-WA1/2020, ( $IC_{50}$  = 31  $\mu$ M, 95% CI 14.7–66.4) and the two 614G+ clinical strains, USA/MDHP-20/2020 (MD) and USA/DCHP-7/2020 (DC) ( $IC_{50}$  = 28  $\mu$ M, 95% CI 14.9–52.9, and 29  $\mu$ M, 95% CI 8.2–102.3, respectively), in Vero C1008 cells with comparable efficacy to that reported above for reference strain Wuhan-Hu-1. Similarly, SFN inhibited the SARS-CoV-2 Delta ( $IC_{50}$  = 5.6  $\mu$ M, 95% CI 4.1–7.8) and Omicron variants ( $IC_{50}$  = 3.3  $\mu$ M, 95% CI 0.9–11.8) (Supplementary Fig. 1).

We next investigated whether SFN could affect an established virus infection. As shown in Figs. 1c and 2b, SFN effectively inhibited both an HCoV-OC43 and a SARS-CoV-2-Wuhan-Hu-1 infection that had been allowed to replicate in Vero C1008 cells for 24 h before the addition of the drug. The  $IC_{50}$  for both viruses was in the lower micromolar range, 18  $\mu$ M (95% CI 4–84.1) and 13  $\mu$ M (95% CI 8.6–20), respectively. Interestingly, these results show that the virus-specific inhibitory activity, i.e., the TI, of SFN is similar whether the drug is added just before or 24 h after virus inoculation (Figs. 1a, c and 2a, b), suggesting an effect on both extracellular entry and intracellular post-entry viral processes. We also determined whether a single application of SFN could protect from the cytopathic effects (CPE) of subsequent viral infection lasting 4 days. As shown in Fig. 1d, SFN pretreatment of Vero C1008 cells resulted in measurable inhibition of HCoV-OC43 CPE with an  $IC_{50}$  = 21  $\mu$ M (95% CI 9.3–49.3) and TI<sub>50</sub> = 4.

We examined the potential synergistic effects of SFN combined with the anti-viral drug remdesivir, an inhibitor of viral RNA-dependent RNA polymerase reported to shorten the time to recovery in adults who were hospitalized with COVID-19<sup>4</sup>. As shown in Fig. 2e, remdesivir effectively inhibits in vitro replication of SARS-CoV-2 in Vero C1008 cells ( $IC_{50}$  = 4  $\mu$ M) as well as HCoV-OC43, albeit at a higher concentration ( $IC_{50}$  = 22  $\mu$ M) (Fig. 1e). In two-drug combination assays, SFN and remdesivir interacted synergistically at several combination ratios to inhibit replication of both HCoV-OC43 (Fig. 1f) and SARS-CoV-2-Wuhan-Hu-1 (Fig. 2f) at concentrations below the corresponding  $IC_{50}$  for each drug. Finally, to evaluate the role of NRF2 in the antiviral activity of SFN, modified Caco-2 cells with decreased expression of NRF2 were infected with SARS-CoV-2 and treated with SFN. We observed a similar reduction in SARS-CoV-2 viral load after SFN treatment in both control and NRF2 knockdown cells, suggesting that the in vitro antiviral activity of SFN is likely to be mediated through an NRF2-independent pathway (Supplementary Fig. 2).

**Effects of SFN treatment in SARS-CoV-2 infected mice.** To evaluate the ability of SFN treatment to reduce viral titers and inflammation in vivo, K18-hACE2 transgenic male mice were inoculated intranasally with  $8.4 \times 10^5$  tissue culture infectious dose 50 (TCID<sub>50</sub>) of SARS-CoV-2/USA/WA1/2020<sup>21</sup>. In K18-hACE2 mice, the human keratin 18 promoter directs expression of hACE2 to epithelia, allowing entry of SARS-CoV-2 into cells (Supplementary Fig. 3). SFN was administered daily via oral gavage (dose of 30 mg/kg bodyweight) to a subgroup of infected animals starting one day prior to viral inoculation (Fig. 3a). A marked weight loss was observed in the infected animals starting at four days post inoculation. By day 6 post inoculation,

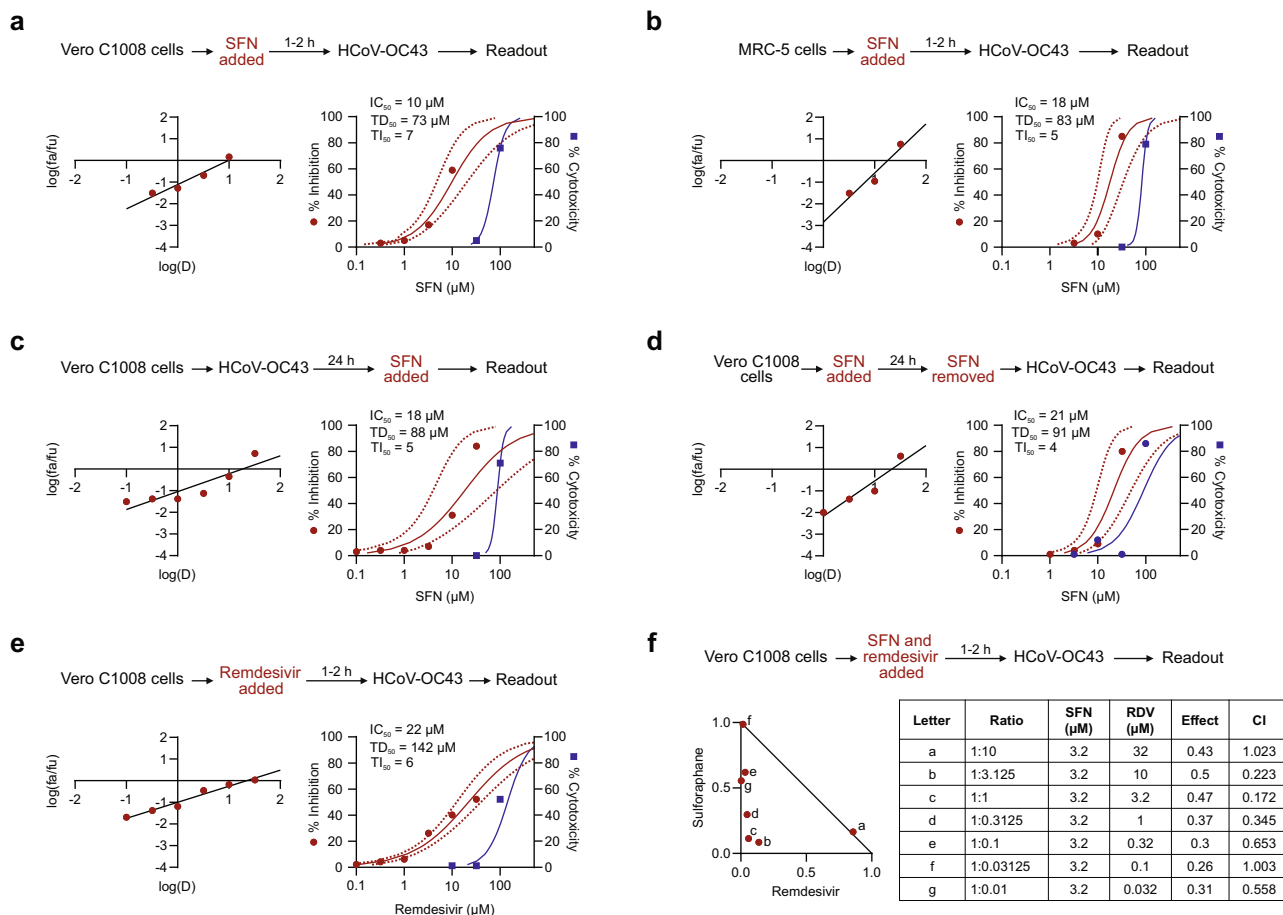


**Fig. 1 Antiviral effects of SFN against HCoV-OC43.** Median effect plots and dose-effect curves calculated for **a** Vero C1008 cells infected with HCoV-OC43 after a 1-2 h incubation with increasing concentrations of SFN; **b** MRC-5 cells infected with HCoV-OC43 after a 1-2 h incubation with increasing concentrations of SFN; **c** Vero C1008 cells infected with HCoV-OC43 over 24 h, after which they were incubated with SFN; **d** Vero C1008 cells incubated with SFN for 24 h, after which the drug was removed, and the cells were infected with HCoV-OC43; **e** Vero C1008 cells infected with HCoV-OC43 after a 1-2 h incubation with increasing concentrations of remdesivir. **f** Normalized isobologram showing combination index (CI) for combinations of various doses. Antiviral data is displayed in red; anti-host cell activity (cytotoxicity) is displayed in blue. Synergism (CI < 1); additive effect (CI = 1); antagonism (CI > 1); SFN, Sulforaphane; RDV, remdesivir. Dotted lines represent 95% confidence interval. Experiments were performed a minimum of 2 times (range = 2-7), 3-6 replicates within each experiment, except experiment shown in **(d)**, which was performed once.

SFN-treated mice lost significantly less weight compared to controls (Fig. 3b,  $P < 0.0001$ ). As a measure of lung injury, the protein concentration in the bronchoalveolar lavage (BAL) was significantly lower in the SFN-treated infected mice compared to untreated infected controls (Fig. 3c,  $P < 0.0001$ ), suggesting a measure of protective effect of drug pretreatment. The viral burden measured in the alveolar fluid was also significantly lower in treated animals compared to untreated controls (Fig. 3d,  $P = 0.04$ ). Similarly, a 1.5 log reduction in viral lung titers was observed in SFN-treated mice compared to untreated controls when normalized to *Pol2Ra* (Fig. 3e,  $P = 0.004$ ). Data on pulmonary viral burden without normalization are presented in Supplementary Fig. 4. Analysis of hematoxylin and eosin-stained lung sections from these animals showed an inflammatory process similar to what has been previously described for this model after SARS-CoV-2 infection<sup>21-23</sup> (Fig. 3f). SFN-treated mice had a lower degree of pulmonary pathology with less alveolar and peribronchiolar inflammation compared to infected untreated mice (Supplementary Fig. 5). Histopathology analysis showed a significant reduction of lung inflammation in SFN-treated mice (histopathology score of 1/16) over untreated controls (histopathology score of 6/16) (Fig. 3g,  $P = 0.0008$ ). Immunostaining for SARS-CoV-2 spike protein revealed a more widespread

distribution in the lungs of infected untreated animals compared to a focal distribution in those of treated animals (Fig. 3f and Supplementary Fig. 5). Quantification of the SARS-CoV-2 spike protein immunostaining revealed that the lung area associated with the virus was 4.4x higher in the infected untreated animals compared to the SFN-treated mice (Fig. 3h,  $P = 0.01$ ).

**Effects of SFN treatment in the immune response.** Given the known immunomodulatory effects of SFN, we employed high-dimensional flow cytometry to evaluate the changes in the immune response of SARS-CoV-2-infected mice treated with SFN and untreated controls, as compared to uninfected mice (Supplementary Fig. 6). Although the immunological landscape was altered as a result of the infection, there were limited differences in overall immune cell composition in the spleen or lungs between treated and untreated mice as visualized using Uniform Manifold Approximation and Projection (UMAP) (Fig. 4a). While changes in the systemic immune responses reflected in the spleen were minimally different (Fig. 4b, c), there were more pronounced effects locally within the lung (Fig. 4b, d). Notably, SARS-CoV-2 infection induced significant recruitment of myeloid cells, including monocytes and dendritic cells, into the

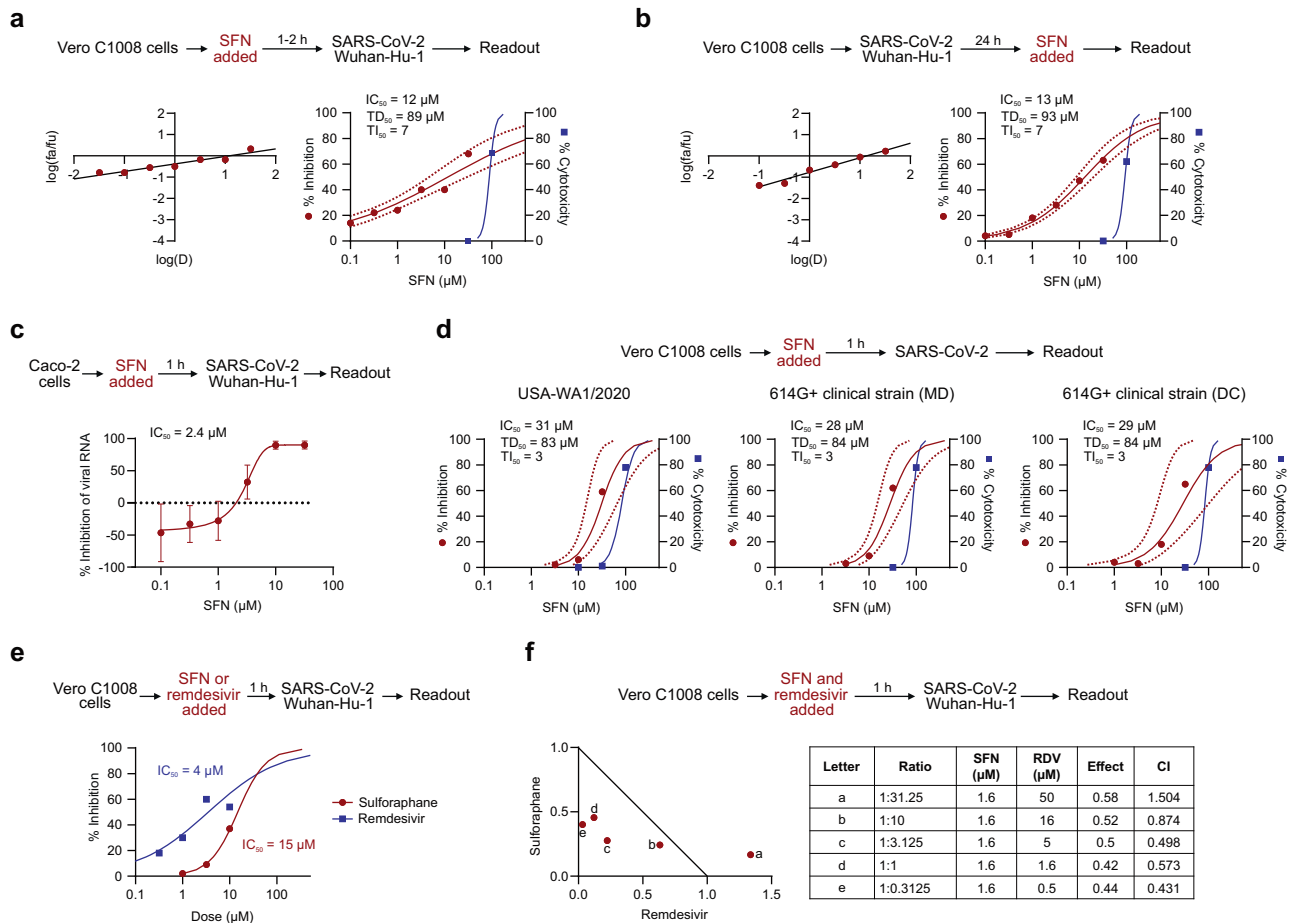


**Fig. 2 Antiviral effects of SFN against SARS-CoV-2.** Median effect plot and dose-effect curves calculated for **a** Vero C1008 cells infected with SARS-CoV-2/Wuhan-Hu-1 after 1-2 h incubation with increasing concentrations of SFN; **b** Vero C1008 cells infected with SARS-CoV-2/Wuhan-Hu-1 for 24 h and then incubated with SFN. Antiviral data is displayed in red; anti-host cell activity (cytotoxicity) is displayed in blue. **c** The antiviral activity in human Caco-2 cells was determined by measuring viral RNA by qPCR. The cells were incubated with SFN for 1 h before viral inoculation. **d** Effects of SFN evaluated in Vero C1008 cells exposed to drug for 1 h followed by viral inoculation. A reference strain (USA-WA1/2020) and two 614G+ clinical strains of SARS-CoV-2 were evaluated for CPE using a bioluminescence readout. **e** Effects of SFN and remdesivir evaluated in Vero C1008 cells exposed to the drug for 1 h followed by viral inoculation. **f** Normalized isobologram showing combination index (CI) for combinations of various doses of SFN and remdesivir. Synergism (CI < 1); Additive effect (CI = 1); Antagonism (CI > 1); SFN, Sulforaphane; RDV, Remdesivir. Dotted lines represent 95% confidence interval. Experiments were performed a minimum of two times (range = 2-7), 3-6 replicates within each experiment, except the experiment shown in **(e)**, which was performed once.

lungs of infected mice. However, SFN-treatment significantly reduced this recruitment compared to infected untreated mice (Fig. 4d,  $P < 0.04$ ). Recruitment of blood monocytes into the lung is known to initiate and maintain lung inflammatory responses, including ARDS, and has been demonstrated in SARS-CoV-2 infection<sup>24</sup>. SFN treatment significantly decreased the percentage of monocytes and CD11c<sup>+</sup> dendritic cells out of total CD45<sup>+</sup> immune cells in the lungs (Fig. 5a,  $P = 0.01$ ). Further, metabolically distinct CPT1a<sup>+</sup>VDAC<sup>+</sup> myeloid cells that have been shown to correlate with disease severity in patients with COVID-19<sup>25</sup> were significantly decreased in response to SFN treatment (Fig. 5a,  $P = 0.01$ ). Alveolar and interstitial macrophages from the lung of SFN-treated mice displayed lower expression of activation markers such as CD80, CD86, PD-L1, and MHC-II (Fig. 5b and Supplementary Fig. 7a, b). Activation also induced significantly lower frequencies of lung alveolar and interstitial macrophages producing cytokines such as IL-10, IL-1β, TNF-α, and TGF-β (Fig. 5c and Supplementary Fig. 7b,  $P < 0.05$ ). These findings were largely replicated in the bronchoalveolar lavage (Supplementary Fig. 8). Together, these data highlight the overall reduction of the local myeloid immune responses within the lung

microenvironment as a result of SFN treatment. In line with the myeloid compartment, T cell activation was also diminished in response to SFN treatment. Directly ex vivo, CD8<sup>+</sup> and CD4<sup>+</sup> T cells isolated from the lung of infected untreated mice demonstrated increased expression of activation markers PD1 and MHC-II and the proliferation marker Ki-67, all of which were significantly decreased in SFN-treated mice (Fig. 5d,  $P < 0.05$ ). This effect on T cell activation was predominantly seen in the lungs and was not found systemically in the spleen. Following stimulation with PMA/ionomycin, CD4<sup>+</sup> T cells from the lung, but not the spleen, produced lower levels of IFN-γ and IL-10; however, the frequency of IL-4 and IL-17 was not significantly altered (Fig. 5e and Supplementary Fig. 9). In summary, the immune-modulatory effects of SFN had a local effect of limiting immune cell activation within the lung without disturbing or substantially altering systemic immune responses in the spleen.

**Discussion**

The ongoing SARS-CoV-2 pandemic has created the immediate need for effective therapeutics that can be rapidly translated to

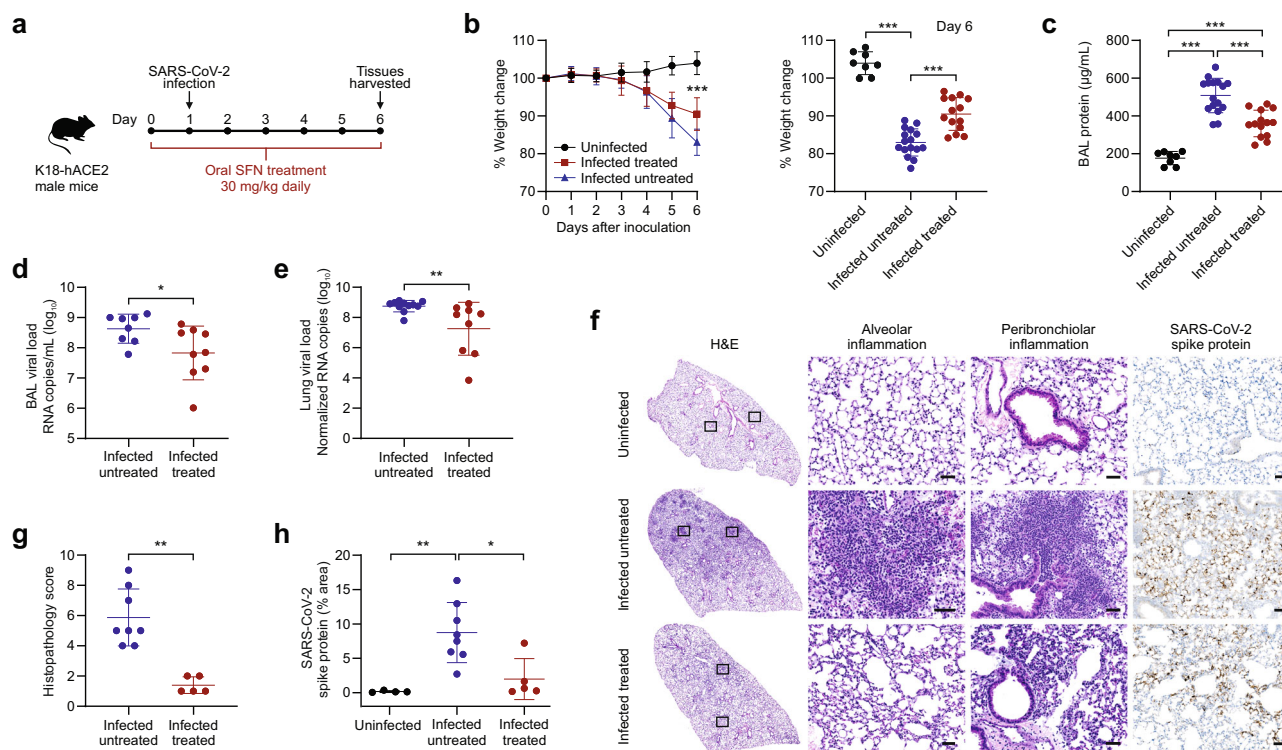


**Fig. 3** SFN treatment in SARS-CoV-2 infected K18-hACE2 mice. **a** Six- to eight-week-old male K18-hACE-transgenic mice were randomly distributed among treatment groups and inoculated intranasally with SARS-CoV-2/USA/WA1/2020 or vehicle. **b** Four days post inoculation, there was a marked weight loss in the infected groups, although there was significantly less weight loss in the SFN treated animals. By day 6 post inoculation, the SFN-treated animals had lost 7.5% less bodyweight compared to infected untreated controls (one-way ANOVA,  $***P < 0.0001$ ). Data from three independent experiments, uninfected ( $n = 8$ ), infected untreated ( $n = 16$ ), infected treated ( $n = 14$ ). **c** Bronchoalveolar lavage (BAL) total protein quantification, determined as a surrogate for lung injury, measured 6 days post-infection. Infected untreated animals had significantly higher total protein compared to the infected treated group (one-way ANOVA,  $***P < 0.0001$ ). Data from three independent experiments, uninfected ( $n = 8$ ), infected untreated ( $n = 16$ ), infected treated ( $n = 14$ ). **d** The viral load in the BAL, as determined by qPCR, was significantly higher in infected untreated animals compared to the infected treated group (Mann-Whitney  $U$  test, two-tailed,  $*P = 0.036$ ). Data from two independent experiments, infected untreated ( $n = 8$ ), infected treated ( $n = 9$ ). **e** The viral load in the lungs of infected treated animals, represented as the SARS-CoV-2 N protein copies normalized to *Pol2Ra*, had a 1.5 log<sub>10</sub> reduction compared to infected untreated controls (Mann-Whitney  $U$  test, two-tailed,  $**P = 0.004$ ). Data from two independent experiments, infected untreated ( $n = 11$ ), infected treated ( $n = 9$ ). **f** Hematoxylin and eosin (H&E) staining and immunostaining for SARS-CoV-2 spike protein of histological sections of the lungs of representative uninfected control, infected untreated and infected treated mice. Regions of the lung anatomy where alveolar and peribronchiolar inflammation was assessed are highlighted in boxes. Images show low (left panels; scale bar, 1 mm) and high-power magnification (right panels; scale bar, 50  $\mu$ m) of the same tissue section. **g** Histopathological severity scoring was evaluated according to the pathological changes outlined in the methods section. Data from one independent experiment, infected untreated ( $n = 8$ ), infected treated ( $n = 5$ ). Mann-Whitney  $U$  test, two-tailed,  $**P = 0.0008$ . **h** Quantification of the SARS-CoV-2 spike protein immunostaining showed a 4.41 $\times$  lower % area in the lungs of SFN-treated mice compared to infected untreated controls ( $P = 0.01$ ). Data from one independent experiment, uninfected ( $n = 4$ ), infected untreated ( $n = 8$ ), infected treated ( $n = 5$ ). One-way ANOVA,  $*P < 0.05$ ,  $**P < 0.005$ . All the data in this figure are represented as mean  $\pm$  standard deviation. Each dot represents one animal.

clinical use. Despite the introduction of vaccines, effective antiviral agents are still necessary, particularly considering the potential effects of viral variants<sup>26</sup>. New oral antivirals targeting viral enzymes (e.g., molnupiravir and Paxlovid) have recently been approved or are in the process of review for emergency use approval by regulatory agencies, with many more currently under development<sup>7,8,27</sup>. However, this approach can be affected by the emergence of viral variants that change the affinity of the drug to the viral protein<sup>28</sup>. An alternative approach is to target host mechanisms required by the virus to infect cells and replicate<sup>29</sup>. Host-directed therapy is advantageous as it allows preexisting drugs to be repurposed, may provide broad-spectrum inhibition against multiple viruses, and is generally thought to be more refractory to viral escape mutations<sup>30,31</sup>.

Following exploratory experiments using the in vitro CPE inhibition assay, SFN was identified as a promising candidate to target the host cellular response, given that it is orally

bioavailable, commercially available at low cost, and has limited side effects<sup>18,32</sup>. We observed that SFN has dual antiviral and anti-inflammatory properties against coronaviruses. We determined that SFN has potent antiviral activity against HCoV-OC43 and multiple strains of SARS-CoV-2, including Delta and Omicron, with limited toxicity in cell culture. The similar results observed between the coronaviruses evaluated suggest that SFN could have broad activity against coronaviruses, a feature that may prove invaluable as new strains of pathogenic coronaviruses enter the human population. Moreover, synergistic antiviral activity was observed in vitro between SFN and remdesivir against both types of coronaviruses tested; comparable synergism in vivo would be advantageous in clinical scenarios where remdesivir is currently being used. We demonstrated in vivo efficacy of prophylactic SFN treatment using the K18-hACE2 mouse model of SARS-CoV-2 infection<sup>22</sup>. Prophylactic SFN-treatment in animals reduced viral replication in the lungs by 1.5

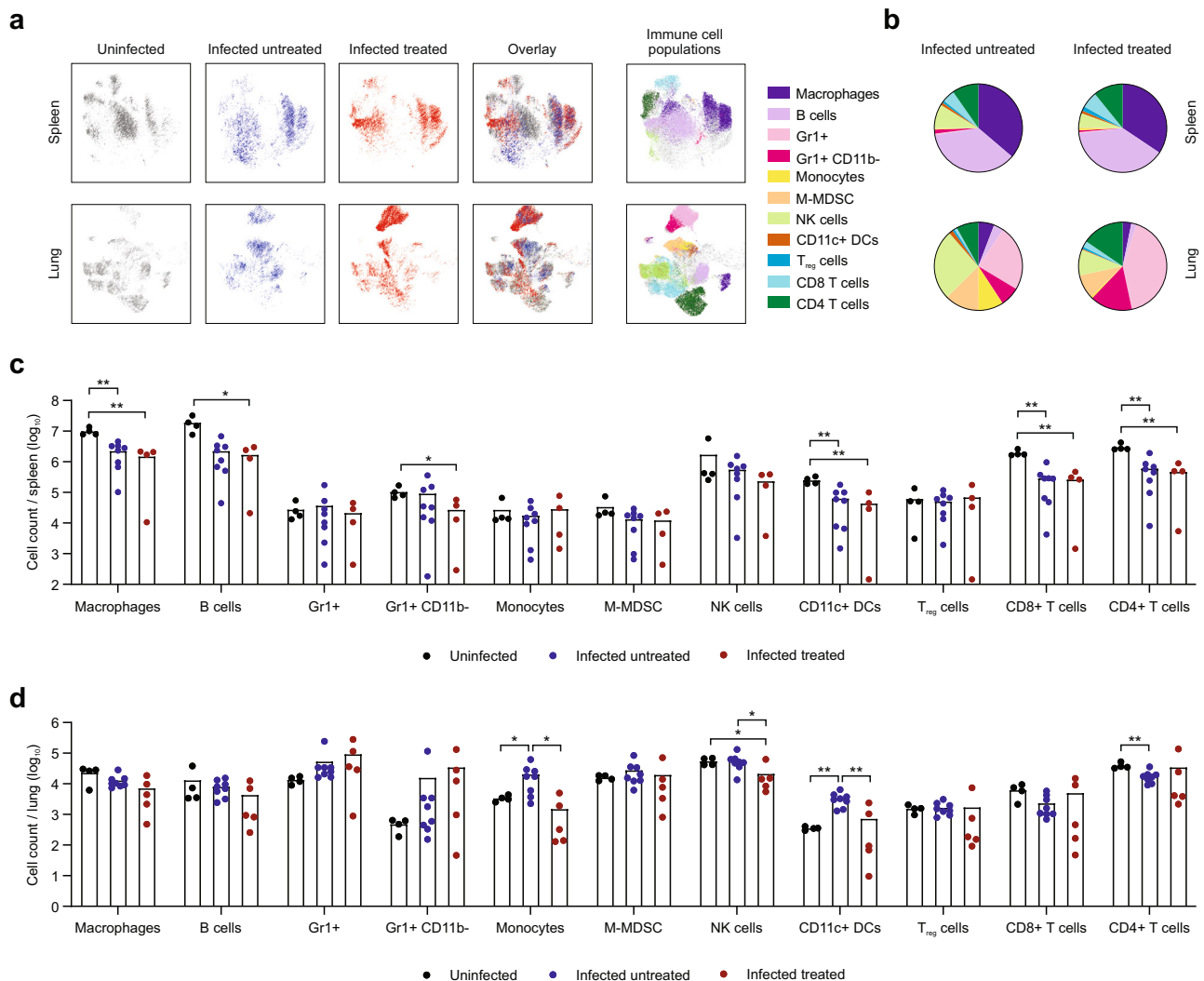


**Fig. 4** Effects of SFN treatment in the immune response. **a** Uniform Manifold Approximation and Projection (UMAP) was used to visualize all the immune cell populations within the spleen and lung of uninfected (grey), infected untreated (blue), and infected treated (red) mice. The corresponding immune cell populations are presented in multiple colors in the panels on the right (**b**). Summary of immune cell frequencies out of total CD45<sup>+</sup> immune cells in spleen and lung of infected treated or untreated mice. **c** Total cell count of indicated immune cell subset per spleen. Each dot represents one mouse. **d** Total cell count of indicated immune cell subset per lung. Each dot represents one mouse, data from one independent experiment. Bars represent mean values. DCs, dendritic cells; NK, natural killer, M-MDSC, mononuclear myeloid-derived suppressor cells. Statistical comparisons were made with two-way ANOVA, \* $P < 0.05$ , \*\* $P < 0.01$ .

orders of magnitude, similar to that reported for remdesivir in the same mouse model<sup>33</sup>. By comparison, BALB/c mice infected with mouse-adapted SARS-CoV-2 had a 1.4 log<sub>10</sub> reduction in viral titers when treated with 300 mg/kg of nirmatrelvir 4 h after infection<sup>8</sup>. As expected, SFN treatment also modulated the inflammatory response in SARS-CoV-2-infected mice, leading to decreased lung injury.

The pathogenesis of many viral infections is associated with increased production of reactive oxygen species (ROS), which leads to cell death<sup>34–36</sup>. Conversely, SFN increases antioxidant, anti-inflammatory, and antiviral defenses through multiple mechanisms<sup>1,7</sup>, including the activation of the cap'n'collar transcription factor NRF2<sup>37</sup>. Under normal conditions, NRF2 remains in an inactive state by association with its inhibitor protein Kelch-like ECH-associated protein 1 (KEAP1)<sup>38</sup>. In response to oxidative stress, KEAP1 is inactivated, and NRF2 is released to induce NRF2-responsive genes that subsequently protect against stress-induced cell death<sup>39</sup>. SFN has been extensively studied in humans for its anti-cancer properties, has been

shown to activate the NRF2 pathway in upper airways<sup>40</sup>, and improves the phagocytic ability of alveolar macrophages<sup>13</sup>. The dual antiviral and anti-inflammatory properties of SFN have also been previously described for other viral infections. In vitro antiviral activity has been reported against influenza virus<sup>41</sup>, and SFN treatment significantly limited lung viral replication and virus-induced inflammation in respiratory syncytial virus-infected mice<sup>42</sup>.

SFN also inhibits inflammation through NRF-2 independent pathways, such as reducing the proinflammatory nuclear factor kappa B (NF- $\kappa$ B)<sup>43</sup>. NF- $\kappa$ B activation has been described as a key component of the inflammatory response to multiple viral infections, including COVID-19<sup>44</sup>. There are also other pathways affected by SFN (e.g., STING, STAT3, macrophage migration inhibitory factor) that could play a role in its antiviral response to coronaviruses<sup>45</sup>. While NRF-2 activation and enhanced transcription of its target genes usually require longer periods of time, we observed potent antiviral activity in cells that had been treated with SFN for only 1–2 h. In NRF2-KD cells infected with SARS-

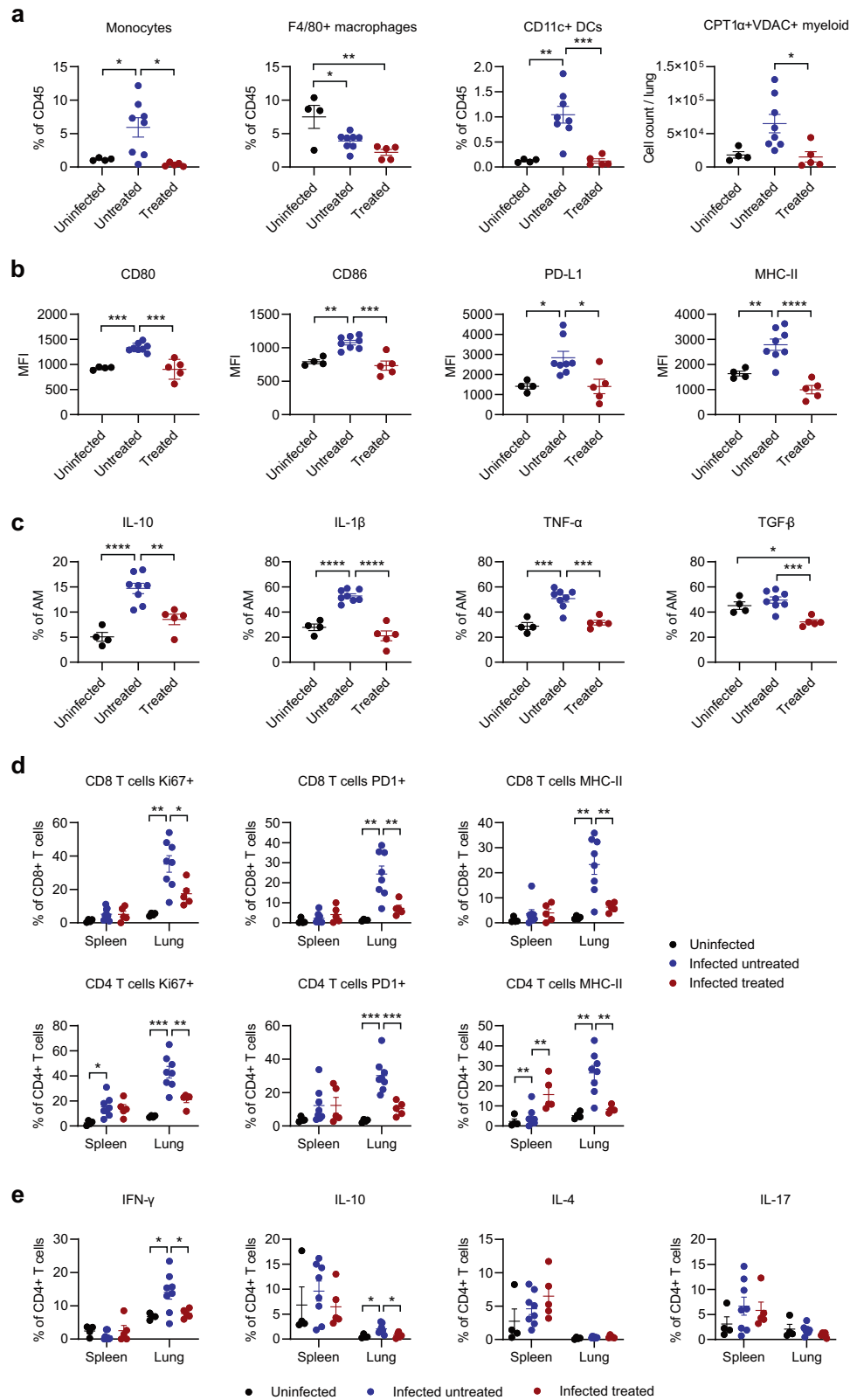


**Fig. 5 Functional characterization of the immune response after SFN treatment.** **a** Myeloid cell subsets shown as percent of total CD45<sup>+</sup> immune cells within the lung. **b** Alveolar macrophages (AM) after stimulation with protein transport inhibitors. MFI, mean fluorescent intensity. **c** Cytokine expression in alveolar macrophages after stimulation with protein transport inhibitors. **d** T cells were stained ex vivo immediately without further stimulation and evaluated for the expression of Ki67, PD1, and MHC-II. Percent of CD8<sup>+</sup> or CD4<sup>+</sup> T cells from spleen or lung expressing indicated marker are shown. **e** Percent of CD8<sup>+</sup> or CD4<sup>+</sup> T cells from spleen or lung expressing indicated marker after stimulation with PMA/ionomycin. Each dot represents one mouse. Data from one independent experiment, uninfected ( $n=4$ ), infected untreated ( $n=8$ ), infected treated ( $n=5$ ). Data represented as mean  $\pm$  standard error of mean. Statistical comparisons were made with one-way ANOVA, \* $P < 0.05$ , \*\* $P < 0.01$ , \*\*\* $P < 0.001$ , \*\*\*\* $P < 0.0001$ .

CoV-2, SFN treatment was still able to significantly reduce the viral load. Therefore, it is possible that the antiviral effect of SFN is NRF-2 independent while the anti-inflammatory effects are mediated primarily by NRF2. Further studies are needed to determine the contribution of each of the different cellular pathways to the antiviral activity of SFN.

As a potent NRF2 activator, SFN can modulate the host's immune response while also providing direct, NRF2-independent antiviral effects. Targeting the NRF2 pathway has been considered a promising approach to develop therapeutics for COVID-19 for multiple reasons<sup>46–48</sup>. NRF2 deficiency is known to upregulate the angiotensin-converting enzyme 2 (ACE2), the primary mechanism of cell entry for SARS-CoV-2. The NRF2 activator oltipraz reduces ACE2 levels, suggesting that NRF2 activation might reduce the availability of ACE2 for SARS-CoV-2 entry into the cell<sup>49</sup>. Increased NRF2 activity also reportedly inhibits IL-6 and IL-1 $\beta$  gene expression<sup>50</sup>, two cytokines known to play key roles in promoting the hyperactive immune response in severely ill COVID-19 patients<sup>51</sup>. Conversely, NRF2 activity is dysregulated in disease states that have been associated with increased severity of COVID-19 (e.g., diabetes)<sup>52</sup>. Further, NRF2 activity declines in older patients who are more susceptible to severe COVID-19<sup>53</sup>. Recent reports suggest that NRF2-dependent genes are suppressed in SARS-CoV-2 infected cells and lung biopsies from COVID-19 patients<sup>46</sup>. Similarly, treatment of cells with NRF2 agonists 4-octyl-itaconate and dimethyl fumarate inhibited replication of SARS-CoV-2 in vitro<sup>46</sup>.

In contrast to therapeutics that inhibit a single cytokine (e.g., IL-6, IL-1 $\beta$ , etc.)<sup>5,54</sup>, SFN has important and diverse effects in modulating the lung immune response to SARS-CoV-2 infection. Excessive inflammatory response to SARS-CoV-2 leads to severe disease or death in patients with COVID-19<sup>55</sup>. Therefore, promoting a balanced and robust antiviral response while modulating excessive innate inflammatory responses could represent a favorable scenario that could reduce viral load while also limiting collateral damage to the infected lung. As has been previously reported, SARS-CoV-2 infection leads to an increase in pulmonary dendritic cells and a reduction in CD4<sup>+</sup> T cells in K18-hACE2 mice<sup>22</sup>. We observed substantial accumulation of immune cells in the lungs of SARS-CoV-2 infected mice, consistent with what has been noted on postmortem analysis of patients with COVID-19<sup>22,56</sup>, as well as decreased numbers of T cells in the spleen, consistent with human studies where lymphopenia is correlated with severe COVID-19<sup>57</sup>. SFN treatment had significant effects on multiple immune cell populations in the lungs, with a reduction in monocytes, NK cells, and dendritic cells compared to infected untreated controls. These findings are likely the effect of a combination of the overall reduced inflammation and direct effects of SFN on specific cell populations. For example, NK cells exposed to SFN had increased cell lytic function through dendritic cell-mediated IL-12 production<sup>58</sup>. We observed decreased recruitment of myeloid cells to the lungs of treated mice and decreased activation profile of local macrophages. The presence of alveolar macrophages with transcriptionally upregulated inflammatory genes and increased secretion of IL-1 $\beta$  have been associated with worse outcomes and increased mortality in patients with ARDS<sup>24,59–61</sup>. Our results show increased IL-1 $\beta$  in alveolar macrophages with SARS-CoV-2 infection, which was abrogated by SFN treatment ( $P < 0.0001$ ). Mechanistically, the benefits of SFN therapy in our model could be due in part to its modulatory effects on myeloid cells after SARS-CoV-2 infection. SFN treatment led to a reduction in TNF- $\alpha$  in alveolar macrophages and IFN- $\gamma$  in T cells, both of which are key triggers of cell death and mortality in SARS-CoV-2 infection and cytokine shock syndromes<sup>62</sup>. Further, SFN was able to reduce but not eliminate T cell activation within the lung. This reduction

in T cell activation could be a direct effect in T cells or could operate through downregulation of myeloid costimulatory for T cells such as CD80/CD86. SFN might therefore be able to modulate and dampen immune responses without inhibiting immunity necessary for viral clearance.

While the K18-hACE2 mouse model has been previously used to recapitulate features of COVID-19 in humans<sup>22</sup>, our study has several limitations. The expression of the hACE2 transgene is non-physiological, resulting in tissue expression levels that are distinct from endogenously expressed ACE2. Sex differences, which are known to occur with SARS-CoV-2 infection, could not be assessed since only male animals were used in these experiments<sup>63,64</sup>. Finally, the absorption of SFN after oral administration can be modified by the intestinal microbiome<sup>10</sup>, leading to potentially variable drug exposures between animals.

Our results demonstrate that pharmacologically relevant micromolar concentrations of SFN inhibited viral replication and virus-induced cell death in vitro. Consumption of SFN-rich broccoli sprouts (single oral daily dose equivalent to 200  $\mu$ mol of SFN) results in a peak plasma concentration ( $C_{max}$ ) of 1.9  $\mu$ M at 2–3 h<sup>65,66</sup>, and higher steady-state levels could be achieved by administering the same dose in two divided doses<sup>10,65,67</sup>. By comparison, SFN inhibited in vitro SARS-CoV-2 replication in human cells with an  $IC_{50}$  of 2.4  $\mu$ M. It is important to note that the bioavailability of SFN in humans is dependent on many factors including amount consumed, dietary form and preparation technique, and the individual's gastrointestinal microflora<sup>10,68,69</sup>. Studies using SFN-rich broccoli sprouts corresponding to 50–400  $\mu$ mol SFN daily have shown that SFN is well tolerated without clinically significant adverse effects<sup>10,32,70,71</sup>. Additionally, while SFN is rapidly eliminated from plasma, it reportedly exerts a sustained effect on gene expression<sup>72</sup>. A daily dose of SFN-rich broccoli sprouts corresponding to 400  $\mu$ mol (70 mg) of SFN in humans is not equivalent to the 30 mg/kg of SFN used in the current mouse studies. Thus, while our results are promising, additional studies in humans are needed to determine the efficacy of SFN as a therapy for COVID-19<sup>68</sup>.

In summary, we documented that SFN can inhibit in vitro and in vivo replication of SARS-CoV-2 at pharmacologically and potentially therapeutically achievable concentrations. Further, it can modulate the inflammatory response, thereby decreasing the consequences of infection in mice when administered prior to infection. Given that SFN is orally bioavailable, commercially available, and has limited side effects, our results suggest it could be a promising approach for the prevention and treatment of COVID-19 as well as other coronavirus infections. Further studies are needed to address these possibilities.

## Methods

**Drugs.** L-SFN, 10 mg/mL in ethanol (56 mM), was obtained from Cayman Chemical (Ann Arbor, MI). D,L-SFN was obtained from Millipore Sigma (St. Louis, MO), and a stock solution of 5 mM was prepared in DMSO. Remdesivir was obtained from MedChemExpress or Cayman Chemical, and stock solutions, 5 or 20 mM, respectively, were prepared in DMSO. Drug stock solutions were stored at  $-25^{\circ}\text{C}$ .

**Cells and viruses.** All cells were obtained from the American Type Culture Collection (ATCC, Manassas, VA, USA) and, with the exception of the Vero C1008 cells derived from African green monkeys, are of human origin (Supplementary Table 2). HCT-8 [HRT-18] (ATCC CCL-244) and Vero C1008 [Vero 76, clone E6, Vero E6] (ATCC CRL-1586) cells were used for growing virus stocks and determining stock titers. Vero C1008 cells, MRC-5 (ATCC CCL-171) cells, and Caco-2 (ATCC HTB-37) cells were used as host cells in antiviral assays. HCT-8 cells were grown in RPMI-1640 medium supplemented with 10% fetal bovine serum (FBS) (MilliporeSigma, St. Louis, MO, USA), L-glutamine, penicillin-streptomycin, and sodium pyruvate. Vero C1008 and MRC-5 cells were grown in Eagle's Minimum Essential Medium (EMEM) with 10% FBS, L-glutamine, and penicillin-streptomycin at  $37^{\circ}\text{C}$  with 5%  $\text{CO}_2$ . Caco-2 cells were grown in EMEM



supplemented with 10% FBS, 1× sodium pyruvate, L-glutamine, and penicillin-streptomycin at 37 °C with 5% CO<sub>2</sub>.

Human coronavirus OC43 (HCoV-OC43) was purchased from ATCC (Betacoronavirus 1, ATCC VR-1558). SARS-CoV-2/Wuhan-1/2020 virus (U.S. Centers for Disease Control and Prevention) was provided by Dr. Andrew Pekosz (Johns Hopkins). 2019-nCoV/USA-WA1/2020 was obtained through BEI Resources, National Institute of Allergy and Infectious Diseases (NIAID), National Institutes of Health. Two 614G+ clinical strains of SARS-CoV-2, SARS-CoV-2/USA/DCHP-7/2020 (DC), and SARS-CoV-2/USA/MDHP-20/2020 (MD) were isolated from patients at The Johns Hopkins Hospitals<sup>73</sup>. The Delta (SARS-CoV-2/USA/MD-HP05660/2021) and Omicron (SARS-CoV-2/USA/MD-HP20874/2021) variants were also isolated from patients as previously described and provided by Dr. Andrew Pekosz. The virus stocks were stored at -80 °C, and titers were determined by tissue culture infectious dose 50 (TCID<sub>50</sub>) assay. All work with infectious SARS-CoV-2 was performed in Institutional Biosafety Committee approved BSL3 and ABSL3 facilities at Johns Hopkins University School of Medicine using appropriate positive pressure air respirators and personal protective equipment.

**CRISPR/Cas9 knockdown and Western blot.** For the generation of the NRF2 KD cells, Caco-2 cells were co-transfected with NRF2-specific CRISPR/Cas9 (sc-400017) and HDR plasmids (sc-400017-HDR) using the UltraCruz<sup>®</sup> Transfection Reagent (sc-395739), as recommended by the manufacturer (Santa Cruz Biotechnology). Control cells were transfected with the HDR plasmid. Cells were selected for 2 weeks with media containing puromycin (3 µg/ml). NRF2 knockdown efficiency was assayed by Western blot<sup>74</sup> using an NRF2 antibody from Abcam (1:1000 dilution, ab62352).

**Cytopathic effect (CPE) inhibition assay.** We employed an assay protocol that interrogates both antiviral and anti-host cell activities to evaluate compounds<sup>75</sup>. This assay is predicated upon the virus's ability to cause a CPE, measured in TCID<sub>50</sub>. Host cells, 7.5–10 × 10<sup>3</sup> in virus growth medium (VGM; Dulbecco's Modified Eagle Medium without phenol red supplemented with 3% FBS), were plated in clear 96-well half-area tissue cultures plates or white, clear-bottom 96 well plates, 24 h prior to the assay. On the day of the assay, working solutions of drugs (0.1–1 mM) were made by dilution of drug stocks in VGM. For one-drug analysis assays, 50 µL of the drug working solution was added to each well in the first column of cells, and then drugs were serially diluted across the plate by dilutions of 0.5 log<sub>10</sub>. The default drug test range was 0.032–320 µM. Drug-exposed cells were incubated for 1–24 h at 35 °C (HCoV-OC43) or 37 °C (SARS-CoV-2), after which time 32 (HCoV-OC43; SARS-CoV-2) or 50 (SARS-CoV-2) TCID<sub>50</sub> of virus suspended in VGM or VGM alone was added to cells. Test plates had virus control wells (virus+/drug-), drug control wells (virus-/drug+), and cell control wells (virus-/drug-). After 3–4 days incubation at 35 °C or 37 °C/5% CO<sub>2</sub>, the cell viability was assessed using CellTiter 96<sup>®</sup> AQueous One Solution (Promega Corp, WI, USA) or CellTiter-Glo<sup>®</sup> One Solution Assay system (Promega) following manufacturer protocols. Color reactions were read at 490–650 nm absorbance in a Filtermax F5 microplate reader (Molecular Devices, CA, USA) using SoftMax Pro 6.5 software. Luminescence readouts were obtained in a FLUOstar Omega plate reader (BMG Labtech, Ortenberg, Germany). For two-drug combination assays, one test drug was serially diluted across the plate (left to right) as described above; the second drug was serially diluted down the plate (top to bottom). The starting concentration of the first drug was adjusted to allow for dilution with the second drug. For interrogation of a drug's ability to affect an established viral infection, host cells were infected with the virus and allowed to incubate for 24 h. After this time, drug dilutions that resulted in the concentration ranges mentioned above, or VGM only, were added to appropriate wells. Cell viability reagent was added at 3–4 days post-infection. For examination of a drug's ability to prevent an infection by pretreatment of the host cells, the test drug was serially diluted across the plate as described above. After 24 h incubation, the drug was removed by aspiration, the cells were rinsed once with warm Hanks' Balanced Salt Solution, and then 32 TCID<sub>50</sub> of virus in drug-free VGM was added to appropriate wells. Cell viability reagent was added at 4 days post-infection.

**In vitro data analysis.** Calcsyn software (Biosoft, Cambridge, UK) was used to calculate the median inhibitory concentration (IC<sub>50</sub>), median cytotoxic dose (TD<sub>50</sub>), and to generate median effect plots and dose-response curves. The therapeutic index (TI), a measure of antiviral selectivity, was calculated by the formula TI = TD<sub>50</sub>/IC<sub>50</sub>. Combination Indices (CI) for two-drug combination assays were calculated by Calcsyn software. Isobolograms to depict synergistic, additive, and antagonistic combinations were generated by the software.

**Viral RNA determination.** Zymo Quick-RNA Viral 96 Kit (Zymo Research) was used to isolate RNA from cell supernatants according to the manufacturer's protocol. cDNA synthesis was performed using qScript cDNA Supermix containing random hexamers and oligo-dT primers following the manufacturer's protocol (Quanta Biosciences). Real-time quantitative reverse transcription PCR (RT-qPCR) was performed in technical triplicate for each sample using TaqMan Fast Advanced Master Mix (Applied Biosystems) on a StepOne Plus Real Time PCR machine

(Applied Biosystems). Primers and probes are listed below. The cycling parameters were as follows: (i) 2 min at 50 °C; (ii) 2 min at 95 °C; and (iii) 45 cycles at 95 °C for 3 s and 55 °C for 30 s. Molecular standard curves were generated using serial dilutions of a plasmid containing the complete SARS-CoV-2 N gene (Integrated DNA Technologies, Catalog #10006625). SARS-CoV-2 RNA was detected using pre-mixed forward (5'-TTACAAACATTGGCCGCGAAA-3') and reverse (5'-GCGGCACATTCCGAAGAA-3') primers and probe (5'-FAM-ACAATTTGCCCCAGCGCTTCAG-BHQ1-3') designed by the U.S. CDC as part of the COVID-19 CDC Research Use Only kit (Integrated DNA Technologies, Catalog #: 10006713) to amplify a region of the SARS-CoV-2 nucleocapsid (N) gene. For lung tissues, the sample was homogenized in 1 mL of TRIzol (Invitrogen), and the RNA was isolated using a combined protocol of TRIzol phenol chloroform and the RNeasy Mini Kit (Qiagen) according to the manufacturer's protocol, and RT-qPCR was performed as described above. For lung tissue lysates, viral copies per lung sample were normalized to the relative expression of the mouse RNA Polymerase II gene (*Pol2Ra*) using the TaqMan gene expression assay (Catalog #: Mm00839502\_m1; ThermoFisher)<sup>76</sup>.

**Animal experiments.** Animal studies were carried out based on the recommendations in the Guide for the Care and Use of Laboratory Animals of the National Institutes of Health. The protocols were approved by the Johns Hopkins University Institutional Animal Care and Use Committee. Heterozygous K18-hACE2 C57BL/6j mice (strain: 2B6.Cg-Tg(K18-ACE2)2Prllm/J) were obtained from The Jackson Laboratory and propagated at Johns Hopkins University School of Medicine. Animals were separately housed in groups and fed standard chow diets. Male mice, 6–8 weeks old, were used for this study. A subgroup of animals received 30 mg/kg daily of SFN diluted in 2% ethanol in water via oral gavage. Treatment started one day prior to viral infection. Infected untreated and uninfected controls also received daily oral gavage with 2% ethanol in water. After induction of anesthesia with ketamine hydrochloride and xylazine, the animals received 8.4 × 10<sup>5</sup> TCID<sub>50</sub> of SARS-CoV-2/USA/WA1/2020 intranasally. Uninfected animals received intranasally the same volume of vehicle. Weights were monitored daily, the animals were sacrificed 6 days post-infection by isoflurane overdose, and the tissues were harvested. Tissues were perfused with PBS after serum collection via cardiac puncture and before tissue harvest. Bronchoalveolar lavage (BAL) was obtained by cannulating the trachea with a 20-gauge catheter. The right lung was lavaged twice (each aliquot 1 ml; calcium-free PBS); total returns averaged 1–1.5 ml/mouse. BAL was centrifuged at 600 × g for 8 min at 4 °C. The cell-free supernatants were stored at -80 °C for total protein quantification using the BCA protein assay (Sigma).

**Flow cytometry.** Lungs were minced and incubated at 37 °C in an enzyme cocktail of RPMI containing 2.4 mg/ml collagenase I and 20 µg/ml DNase (Invitrogen), then mashed through a 70 µm nylon cell strainer (BD Falcon). All flow cytometry antibodies used for phenotypic and metabolic analysis can be found in Supplementary Table 3. For analysis immediately ex vivo, cells were washed once in PBS and immediately stained for viability with Biogend Live/Dead Zombie NIR Fixable Viability Dye and Fc Block for 10 min at room temperature. Cell surface staining was performed in 100 µL of 20% BD Horizon™ Brilliant Stain Buffer plus PBS with surface stain antibody cocktail for 20 min at room temperature. Cells were fixed and permeabilized with eBioscience™ FoxP3/Transcription Factor Staining kit 1× Fixation/Permeabilization reagent overnight at 4 °C. Cells were washed with 1× Permeabilization/Wash buffer. Intracellular staining (ICS) was performed in 100 µL 1× Permeabilization/Wash buffer with ICS antibody cocktail for 45 min at room temperature. Cells were washed once with Permeabilization/Wash buffer then resuspended in Permeabilization/Wash buffer for acquisition by flow. To improve the quality of the T cell flow cytometry functional staining, the cells were stimulated with phorbol 12-myristate 13-acetate (PMA, 50 ng/mL) and ionomycin (1 µg/mL) for 1 h, followed by a 3 h incubation with protein transport inhibitors (GolgiPlug and GolgiStop, BD). For the myeloid flow cytometry functional staining, the cells were incubated only with protein transport inhibitors for 4 h. Samples were run on a 3 laser Cytek Aurora spectral flow cytometer or a FACSAria II spectral flow cytometer (BD). FCS files were analyzed using Flowjo v10.6.2 software (BD). Manual gating strategies for all the panels can be found in Fig. S6. High-dimensional unbiased analysis of cell phenotypes was performed using Flowjo plugins DownSample v3 and UMAP.

**Histology and immunohistochemistry.** After euthanasia, tissues were fixed with 10% neutral-buffered formalin. Tissues were embedded in paraffin, and sections were stained with hematoxylin and eosin. Digital light microscopy scans of the lung were examined implementing a semi-quantitative, 5-point grading scheme (0 - within normal limits, 1 - mild, 2 - moderate, 3 - marked, 4 - severe) based on what has been previously reported by White et al. for this infection model<sup>33</sup>. The scoring system considered four different histopathological parameters: (1) perivascular inflammation, (2) bronchial or bronchiolar epithelial degeneration or necrosis, (3) bronchial or bronchiolar inflammation, and (4) alveolar inflammation. These changes were absent (grade 0) in lungs from uninfected mice. Individual total pathology scores varied from 1/16 to 2/16 for the SFN-treated group and from 4/16 to 9/16 for the infected untreated controls. Immunostaining was performed at the Oncology Tissue Services Core of Johns Hopkins University School of Medicine.

Immunolabeling for the SARS-CoV-2 spike protein was performed on formalin-fixed, paraffin-embedded sections on a Ventana Discovery Ultra autostainer (Roche Diagnostics). Briefly, following dewaxing and rehydration on board, epitope retrieval was performed using Ventana Ultra CCl1 buffer (catalog # 6414575001, Roche Diagnostics) at 96 °C for 64 min. Primary antibody, anti-SARS-CoV-2 spike protein (1:200 dilution; catalog # GTX135356, lot # 43957, Genetex) was applied at 36 °C for 60 min. Primary antibodies were detected using an anti-rabbit HQ detection system (catalog # 7017936001 and 7017812001, Roche Diagnostics) followed by Chromomab DAB IHC detection kit (catalog # 5266645001, Roche Diagnostics), counterstaining with Mayer's hematoxylin, dehydration, and mounting. The primary antibody for hACE2 immunolabeling was recombinant Anti-ACE2 antibody [Catalog # EPR4435(2), ab108252; Abcam]. Automated analysis of the SARS-CoV-2 spike protein immunostaining was performed with Halo v3.2.1851.328 (Indica Labs). The area corresponding to the anti-SARS-CoV-2 spike protein was divided by the sum of the areas corresponding to cellular structures stained with Mayer's hematoxylin and anti-SARS-CoV-2 spike protein. The ratio is represented as a percentage.

**Statistics and reproducibility.** Data were analyzed using Prism 9.2.0 (GraphPad). Specifics of statistical comparisons are detailed in individual figure legends. Statistical significance was assigned when *P* values were <0.05.

**Reporting summary.** Further information on research design is available in the Nature Research Reporting Summary linked to this article.

### Data availability

All data associated with this study are present in the paper or the Supplementary Materials. All source data underlying the graphs presented in the main and supplementary figures are available in Supplementary Data 1.

Received: 15 April 2021; Accepted: 24 February 2022;

Published online: 18 March 2022

### References

- Taylor, P. C. et al. Neutralizing monoclonal antibodies for treatment of COVID-19. *Nat. Rev. Immunol.* **21**, 382–393 (2021).
- Sullivan, D. J. et al. Randomized controlled trial of early outpatient COVID-19 treatment with high-titer convalescent plasma. *medRxiv* <https://doi.org/10.1101/2021.12.10.21267485> (2021).
- Gordon, O. et al. Pharmacokinetics of high-titer anti-SARS-CoV-2 human convalescent plasma in high-risk children. *JCI Insight* **2**, e151518 (2021).
- Beigel, J. H. et al. Remdesivir for the treatment of Covid-19—final report. *N. Engl. J. Med.* **383**, 1813–1826 (2020).
- Shankar-Hari, M. et al. Association between administration of IL-6 antagonists and mortality among patients hospitalized for COVID-19: A meta-analysis. *JAMA* **326**, 499–518 (2021).
- Gupta, A. et al. Early treatment for Covid-19 with SARS-CoV-2 neutralizing antibody sotrovimab. *N. Engl. J. Med.* **385**, 1941–1950 (2021).
- Jayk Bernal, A. et al. Molnupiravir for oral treatment of Covid-19 in nonhospitalized patients. *N. Engl. J. Med.* **386**, 509–520 (2022).
- Owen, D. R. et al. An oral SARS-CoV-2 Mpro inhibitor clinical candidate for the treatment of COVID-19. *Science* **374**, 1586–1593 (2021).
- Cox, R. M., Wolf, J. D. & Plemper, R. K. Therapeutically administered ribonucleoside analogue MK-4482/EIDD-2801 blocks SARS-CoV-2 transmission in ferrets. *Nat. Microbiol.* **6**, 11–18 (2021).
- Yagishita, Y., Fahey, J. W., Dinkova-Kostova, A. T. & Kensler, T. W. Broccoli or sulforaphane: Is it the source or dose that matters? *Molecules* **24**, 3593 (2019).
- Sulforaphane glucosinolate. Monograph. *Alter. Med. Rev.* **15**, 352–360 <https://pubmed.ncbi.nlm.nih.gov/21194251/> (2010).
- Mahn, A. & Castillo, A. Potential of sulforaphane as a natural immune system enhancer: A review. *Molecules* **26**, 752 (2021).
- Harvey, C. J. et al. Targeting Nrf2 signaling improves bacterial clearance by alveolar macrophages in patients with COPD and in a mouse model. *Sci. Transl. Med.* **3**, 78ra32–78ra32 (2011).
- Sun, Z., Niu, Z., Wu, S. & Shan, S. Protective mechanism of sulforaphane in Nrf2 and anti-lung injury in ARDS rabbits. *Exp. Ther. Med.* **15**, 4911–4915 (2018).
- Noah, T. L. et al. Effect of broccoli sprouts on nasal response to live attenuated influenza virus in smokers: A randomized, double-blind study. *PLoS One* **9**, e98671 (2014).
- Houghton, C. A. Sulforaphane: Its “Coming of Age” as a clinically relevant nutraceutical in the prevention and treatment of chronic disease. *Oxid. Med. Cell Longev.* **2019**, 2716870 (2019).
- Cuadrado, A. et al. Can activation of NRF2 be a strategy against COVID-19? *Trends Pharm. Sci.* **41**, 598–610 (2020).
- Axelsson, A. S. et al. Sulforaphane reduces hepatic glucose production and improves glucose control in patients with type 2 diabetes. *Sci. Transl. Med.* **9**, eaah4477 (2017).
- Dickerson, F. et al. Randomized controlled trial of an adjunctive sulforaphane nutraceutical in schizophrenia. *Schizophr. Res.* **231**, 142–144 (2021).
- Zhou, B. et al. SARS-CoV-2 spike D614G change enhances replication and transmission. *Nature* **592**, 122–127 (2021).
- Zheng, J. et al. COVID-19 treatments and pathogenesis including anosmia in K18-hACE2 mice. *Nature* **589**, 603–607 (2021).
- Winkler, E. S. et al. SARS-CoV-2 infection of human ACE2-transgenic mice causes severe lung inflammation and impaired function. *Nat. Immunol.* **21**, 1327–1335 (2020).
- Oladunni, F. S. et al. Lethality of SARS-CoV-2 infection in K18 human angiotensin-converting enzyme 2 transgenic mice. *Nat. Commun.* **11**, 6122 (2020).
- D'Alessio, F. R. & Heller, N. M. COVID-19 and myeloid cells: Complex interplay correlates with lung severity. *J. Clin. Invest.* **130**, 6214–6217 (2020).
- Thompson, E. A. et al. Metabolic programs define dysfunctional immune responses in severe COVID-19 patients. *Cell Rep.* **34**, 108863 (2021).
- Fontanet, A. et al. SARS-CoV-2 variants and ending the COVID-19 pandemic. *Lancet* **397**, 952–954 (2021).
- Sheahan, T. P. et al. An orally bioavailable broad-spectrum antiviral inhibits SARS-CoV-2 in human airway epithelial cell cultures and multiple coronaviruses in mice. *Sci. Transl. Med.* **12**, eabb5883 (2020).
- Mascola, J. R., Graham, B. S. & Fauci, A. S. SARS-CoV-2 viral variants—tackling a moving target. *JAMA* **325**, 1261–1262 (2021).
- Wong, J. P. & Damania, B. SARS-CoV-2 dependence on host pathways. *Science* **371**, 884–885 (2021).
- Bekerman, E. & Einav, S. Combating emerging viral threats. *Science* **348**, 282–283 (2015).
- Wang, R. et al. Genetic screens identify host factors for SARS-CoV-2 and common cold coronaviruses. *Cell* **184**, 106–119.e114 (2021).
- Singh, K. et al. Sulforaphane treatment of autism spectrum disorder (ASD). *Proc. Natl Acad. Sci. USA* **111**, 15550–15555 (2014).
- White, K. M. et al. Plitidepsin has potent preclinical efficacy against SARS-CoV-2 by targeting the host protein eEF1A. *Science* **371**, 926–931 (2021).
- Lee, C. Therapeutic modulation of virus-induced oxidative stress via the Nrf2-dependent antioxidative pathway. *Oxid. Med. Cell Longev.* **2018**, 6208067 (2018).
- Schwarz, K. B. Oxidative stress during viral infection: A review. *Free Radic. Biol. Med.* **21**, 641–649 (1996).
- Siska, P. J. et al. Metabolic imbalance of T cells in COVID-19 is hallmarked by basigin and mitigated by dexamethasone. *J. Clin. Invest.* **131**, e148225 (2021).
- Dinkova-Kostova, A. T. et al. Direct evidence that sulfhydryl groups of Keap1 are the sensors regulating induction of phase 2 enzymes that protect against carcinogens and oxidants. *Proc. Natl Acad. Sci. USA* **99**, 11908–11913 (2002).
- Hayes, J. D. & Dinkova-Kostova, A. T. The Nrf2 regulatory network provides an interface between redox and intermediary metabolism. *Trends Biochem. Sci.* **39**, 199–218 (2014).
- Soares, M. P. & Ribeiro, A. M. Nrf2 as a master regulator of tissue damage control and disease tolerance to infection. *Biochem. Soc. Trans.* **43**, 663–668 (2015).
- Riedl, M. A., Saxon, A. & Diaz-Sanchez, D. Oral sulforaphane increases Phase II antioxidant enzymes in the human upper airway. *Clin. Immunol.* **130**, 244–251 (2009).
- Kesic, M. J., Simmons, S. O., Bauer, R. & Jaspers, I. Nrf2 expression modifies influenza A entry and replication in nasal epithelial cells. *Free Radic. Biol. Med.* **51**, 444–453 (2011).
- Cho, H.-Y. et al. Antiviral activity of Nrf2 in a murine model of respiratory syncytial virus disease. *Am. J. Respir. Crit. Care Med.* **179**, 138–150 (2009).
- Kivelä, A. M. et al. Sulforaphane inhibits endothelial lipase expression through NF-κB in endothelial cells. *Atherosclerosis* **213**, 122–128 (2010).
- Kirchheis, R. et al. NF-κB pathway as a potential target for treatment of critical stage COVID-19 patients. *Front. Immunol.* **11**, 598444 (2020).
- Olagnier, D. et al. Nrf2 negatively regulates STING indicating a link between antiviral sensing and metabolic reprogramming. *Nat. Commun.* **9**, 1–13 (2018).
- Olagnier, D. et al. SARS-CoV2-mediated suppression of NRF2-signaling reveals potent antiviral and anti-inflammatory activity of 4-octyl-itaconate and dimethyl fumarate. *Nat. Commun.* **11**, 4938 (2020).
- Herengt, A., Thyrdsted, J. & Holm, C. K. NRF2 in viral infection. *Antioxidants* **10**, 1491 (2021).
- Forcados, G. E., Muhammad, A., Oladipo, O. O., Makama, S. & Meseko, C. A. Metabolic implications of oxidative stress and inflammatory process in SARS-CoV-2 pathogenesis: Therapeutic potential of natural antioxidants. *Front. Cell Infect. Microbiol.* **11**, 654813 (2021).

49. Zhao, S. et al. Nrf2 deficiency upregulates intrarenal angiotensin-converting enzyme-2 and angiotensin 1-7 receptor expression and attenuates hypertension and nephropathy in diabetic mice. *Endocrinology* **159**, 836–852 (2018).
50. Kobayashi, E. H. et al. Nrf2 suppresses macrophage inflammatory response by blocking proinflammatory cytokine transcription. *Nat. Commun.* **7**, 11624 (2016).
51. Moore, J. B. & June, C. H. Cytokine release syndrome in severe COVID-19. *Science* **368**, 473–474 (2020).
52. Rabbani, P. S. et al. Dysregulation of Nrf2/Keap1 redox pathway in diabetes affects multipotency of stromal cells. *Diabetes* **68**, 141–155 (2019).
53. Schmidlin, C. J., Dodson, M. B., Madhavan, L. & Zhang, D. D. Redox regulation by NRF2 in aging and disease. *Free Radic. Biol. Med.* **134**, 702–707 (2019).
54. Salama, C. et al. Tocilizumab in patients hospitalized with Covid-19 pneumonia. *N. Engl. J. Med.* **384**, 20–30 (2020).
55. Mehta, P. et al. COVID-19: consider cytokine storm syndromes and immunosuppression. *Lancet* **395**, 1033–1034 (2020).
56. Xu, Z. et al. Pathological findings of COVID-19 associated with acute respiratory distress syndrome. *Lancet Respir. Med.* **8**, 420–422 (2020).
57. Wang, F. et al. Characteristics of peripheral lymphocyte subset alteration in COVID-19 pneumonia. *J. Infect. Dis.* **221**, 1762–1769 (2020).
58. Singh, S. V. et al. Sulforaphane inhibits prostate carcinogenesis and pulmonary metastasis in TRAMP mice in association with increased cytotoxicity of natural killer cells. *Cancer Res.* **69**, 2117–2125 (2009).
59. Jacobs, R. F., Tabor, D. R., Burks, A. W. & Campbell, G. D. Elevated interleukin-1 release by human alveolar macrophages during the adult respiratory distress syndrome. *Am. Rev. Respir. Dis.* **140**, 1686–1692 (2012).
60. Donnelly, S. C. et al. Interleukin-8 and development of adult respiratory distress syndrome in at-risk patient groups. *Lancet* **341**, 643–647 (1993).
61. Morrell, E. D. et al. Alveolar macrophage transcriptional programs are associated with outcomes in acute respiratory distress syndrome. *Am. J. Respir. Crit. Care Med.* **200**, 732–741 (2019).
62. Karki, R. et al. Synergism of TNF- $\alpha$  and IFN- $\gamma$  triggers inflammatory cell death, tissue damage, and mortality in SARS-CoV-2 infection and cytokine shock syndromes. *Cell* **184**, 149–168.e117 (2021).
63. Dhakal, S. et al. Sex differences in lung imaging and SARS-CoV-2 antibody responses in a COVID-19 golden Syrian hamster model. *mBio* **12**, e00974–00921 (2021).
64. Bunders, M. J. & Altfeld, M. Implications of sex differences in immunity for SARS-CoV-2 pathogenesis and design of therapeutic interventions. *Immunity* **53**, 487–495 (2020).
65. Atwell, L. L. et al. Absorption and chemopreventive targets of sulforaphane in humans following consumption of broccoli sprouts or a myrosinase-treated broccoli sprout extract. *Mol. Nutr. Food Res.* **59**, 424–433 (2015).
66. Ye, L. et al. Quantitative determination of dithiocarbamates in human plasma, serum, erythrocytes, and urine: Pharmacokinetics of broccoli sprout isothiocyanates in humans. *Clin. Chim. Acta* **316**, 43–53 (2002).
67. Egner, P. A. et al. Rapid and sustainable detoxication of airborne pollutants by broccoli sprout beverage: Results of a randomized clinical trial in China. *Cancer Prev. Res.* **7**, 813–823 (2014).
68. Fahey, J. W. & Kensler, T. W. The challenges of designing and implementing clinical trials with broccoli sprouts... and turning evidence into public health action. *Front. Nutr.* **8**, 648788 (2021).
69. Shapiro, T., Fahey, J., Wade, K., Stephenson, K. & Talalay, P. Human metabolism and excretion of cancer chemoprotective glucosinolates and isothiocyanates of cruciferous vegetables. *Cancer Epidemiol. Biomark. Prev.* **7**, 1091–1100 (1998).
70. Shapiro, T. A. et al. Safety, tolerance, and metabolism of broccoli sprout glucosinolates and isothiocyanates: A clinical phase I study. *Nutr. Cancer* **55**, 53–62 (2006).
71. Yagishita, Y., Gatbonton-Schwager, T. N., McCallum, M. L. & Kensler, T. W. Current landscape of NRF2 biomarkers in clinical trials. *Antioxidants* **9**, 716 (2020).
72. Hu, R. et al. In vivo pharmacokinetics and regulation of gene expression profiles by isothiocyanate sulforaphane in the rat. *J. Pharm. Exp. Ther.* **310**, 263–271 (2004).
73. Gniazdowski, V. et al. Repeat COVID-19 molecular testing: Correlation of SARS-CoV-2 culture with molecular assays and cycle thresholds. *Clin. Infect. Dis.* **73**, e860–e869 (2020).
74. Merino, V. F. et al. Combined treatment with epigenetic, differentiating, and chemotherapeutic agents cooperatively targets tumor-initiating cells in triple-negative breast cancer. *Cancer Res.* **76**, 2013–2024 (2016).
75. Revu, O. et al. Total synthesis of the natural product (+)-trans-dihydronarciclasine via an asymmetric organocatalytic [3+3]-cycloaddition and discovery of its potent anti-Zika virus (ZIKV) activity. *ChemistrySelect* **1**, 5895–5899 (2016).
76. Radonić, A. et al. Guideline to reference gene selection for quantitative real-time PCR. *Biochem. Biophys. Res. Commun.* **313**, 856–862 (2004).

## Acknowledgements

We thank Dr. Andrew Pekosz for providing the viral strains and Sujayita Roy for assisting with IHC staining. We also thank Dr. Jason S. Villano for supporting animal breeding and Drs. Jed W. Fahey and Craig W. Hendrix for valuable expert discussions about this project and manuscript. This study was supported by the National Institutes of Health (R01-AI153349, R01-AI145435-A1, and R21-AI149760 to S.K.J. and A.A.O.), support from the Center for Infection and Inflammation Imaging Research (Johns Hopkins University), Mercatus Center Fast Grant (#2167) to C.K.B., and the Stanley Medical Research Institute (R.H.Y. and L.J.-B.).

## Author contributions

Conceptualization: A.A.O. and L.J.-B. Formal analysis: A.A.O., C.K.B., L.J.-B., A.F.V.-R., E.A.T., V.F.M., J.D.P., and F.R.D. Funding acquisition: R.H.Y., S.K.J., and L.J.-B. Investigation: A.A.O., C.K.B., S.L.D., O.K., A.F.V.-R., M.L.T., E.A.T., V.F.M., Y.Y., J.K., and L.J.-B. Methodology: A.A.O. and L.J.-B. Resources: R.H.Y. and S.K.J. Supervision: A.A.O., L.J.-B., R.H.Y., and S.K.J. Validation: A.A.O., L.J.-B., R.H.Y., and S.K.J. Visualization: A.A.O. Writing - original draft: A.A.O. and L.J.-B. Writing - review & editing: all authors.

## Competing interests

L.J.-B., A.A.O., R.H.Y., and S.K.J. are co-inventors on pending patent application USPA #63/142,598, “Methods for inhibiting coronaviruses using sulforaphane” filed by Johns Hopkins University. All other authors declare no competing interests.

## Additional information

**Supplementary information** The online version contains supplementary material available at <https://doi.org/10.1038/s42003-022-03189-z>.

**Correspondence** and requests for materials should be addressed to Alvaro A. Ordóñez or Lorraine Jones-Brando.

**Peer review information** *Communications Biology* thanks Yongping Bao and the other, anonymous, reviewers for their contribution to the peer review of this work. Primary Handling Editors: Nicolas Fanget and Caitlin Karniski.

**Reprints and permission information** is available at <http://www.nature.com/reprints>

**Publisher's note** Springer Nature remains neutral with regard to jurisdictional claims in published maps and institutional affiliations.



**Open Access** This article is licensed under a Creative Commons Attribution 4.0 International License, which permits use, sharing, adaptation, distribution and reproduction in any medium or format, as long as you give appropriate credit to the original author(s) and the source, provide a link to the Creative Commons license, and indicate if changes were made. The images or other third party material in this article are included in the article's Creative Commons license, unless indicated otherwise in a credit line to the material. If material is not included in the article's Creative Commons license and your intended use is not permitted by statutory regulation or exceeds the permitted use, you will need to obtain permission directly from the copyright holder. To view a copy of this license, visit <http://creativecommons.org/licenses/by/4.0/>.

© The Author(s) 2022